



1 Real-time monitoring and FEMLIP simulation of a rainfall-induced 2 rockslide

3
4 ZhaoHua Li¹, ZhiGang Tao¹, YuanJun Jiang^{2*}, Qian Lv¹, Felix Darve³, ManChao He¹

5
6 1. State Key Laboratory for Geomechanics and Deep Underground Engineering, China University of Mining and
7 Technology, Beijing, 100083, China

8 2. Institute of Mountain Hazards & Environment, Chinese Academy of Sciences, Chengdu, China

9 3. Grenoble CNRS, UMR 5521, 3SR, Grenoble Alpes University, Grenoble, France

10
11 **Abstract.** Rockslides are a common and devastating problem affecting mining and other engineering activities all
12 over the world; consequently, there have been many studies into their prediction and prevention. This study focused
13 on a recent rockslide in an open pit mine in Liaoning province, China. The stability of the rock slope under
14 excavation and rainfall conditions was monitored using an efficient real-time monitoring system. A further
15 numerical analysis was performed using the Finite Element Method with Lagrangian Integration Points (FEMLIP),
16 and the normalized global second order work was implanted to assess the structure instability as a safety factor. In
17 fact for the future it would be very interesting to compare in real time measurements and simulations, and not only
18 to develop back computations after failure. The numerical results indicate that the rock slope remained stable during
19 excavation, yet lost stability after subsequent rainfall. Water infiltration, along with a major geological discontinuity,
20 degraded the strength of the weak zone and induced the rockslide. The monitoring approach presented its robustness
21 and generality, and was worth being generalized. The numerical approach proposed the evolution of the safety factor,
22 comparing the monitoring data, and the mechanism of the rockslide was determined. It could be used as an assistant
23 tool for the disaster predictions.

24
25 **Keywords:** rockslide, second order work, FEMLIP, prediction, landslide monitoring, rainfall.

26 Acknowledgements

27
28 Acknowledgements: This work was supported by the CAS Pioneer Hundred Talents Program, and the Major
29 Program of National Natural Science of Foundation of China (41502334).

30
31
32

*Corresponding author: Yuanjun Jiang, Associated research fellow, PhD, E-mail: lizheng6224166@126.com. Institute of Mountain Hazards & Environment, Chinese Academy of Sciences, 9, Block 4, Renminnanlu Road, Chengdu, 610041, China. TEL: 8628-85228816, Fax: +8628-85222258



1 Introduction

2

3 Rockslides characterized by sudden occurrence, large volume, and frequently high acceleration are a hazard
4 around the world. The mechanisms driving this hazard are complex, and rockslides can be influenced by a large
5 number of factors, including topography, earthquakes, human factors, and climatic variation (Chen et al., 2006;
6 Wang et al., 2011; Tu et al., 2009). Rockslides can occur suddenly and rapidly; for example, after rock slopes
7 undergo a series of slow and imperceptible changes. For civil safety and engineering activities, careful monitoring
8 and accurate predictions are a challenging geological and geotechnical issue.

9

10 Not all rock slope instabilities induce catastrophic consequences. Recently, a sudden rockslide in an open-pit iron
11 ore mine was successfully monitored on October 31, 2016. Early warnings were received, and fatalities and
12 economic damage were avoided. This rockslide occurred after excavation on the toe of slope and subsequent
13 rainfall lasting about 21 hours. The slope was reinforced and stability was monitored using the
14 Constant-Resistance-Large-Deformation (CRLD) cable, which could support a large elongation of 2m, and
15 provide a constant resistance during the large elongation (He, 2009; He et al., 2014). Using real-time monitoring
16 data, the early warning system sent urgent sliding warnings, so that all staff and equipment were evacuated in time.
17 After 4 hours, global instability occurred and a rock mass with a volume of $1.35 \times 10^4 \text{ m}^3$ slid down slope. It should
18 be noted that this rockslide was the second sliding in the same area, and there was another rockslide, induced by
19 excavation and occurred in 2011. It was also successfully predicted using the monitoring system, and the reliability
20 of this monitoring system for excavation-induced rockslides has been proven (Li et al., 2018b). One of the
21 objectives of this study is to present the monitoring of the second rockslide in 2016, and to discuss the adaptability
22 of the monitoring system for rockslides induced by different triggering factors.

23

24 The numerical method is an important tool to analyze the failure mechanisms and the instability issues of
25 geomaterials. Besides the classical Finite Element Methods (FEM) and the Finite Difference Method (FDM),
26 diverse new numerical approaches have been proposed (Soga et al., 2016). Smooth particle hydrodynamics (SPH)
27 (Cascini et al., 2014) has been used to simulate channelized landslides of flow type; the material point method (MPM)
28 (Soga et al., 2016; Abe et al., 2013; Marcelo et al., 2016; Bandara et al., 2016) can describe the whole process of
29 landslide movement using hydro-mechanical coupling; the discrete element method (DEM) has been used to model
30 the instability of jointed rock slopes (Dong et al., 2015; Huang et al., 2015); and the Finite Element Method with
31 Lagrangian Integration Points (FEM-LIP) method (Cuomo et al., 2013) is developed from the particle-in-cell method
32 (PIC) (Harlow 1964; Moresi et al., 2002; Moresi et al., 2003) and satisfies the two requirements for simulating the
33 complete evolution of landslides: precise tracking of internal variables and the ability to solve large displacements
34 (Li et al., 2016; Li et al., 2018a; Prime et al., 2013). In contrast to the material point method, the numerical weight
35 of material particles used in the FEM-LIP method is updated each time step, leading to an acceptable calculation cost,
36 owing to the use of an implicit solver (Li et al., 2018a). Each method has its advantages and drawbacks, and the
37 details can be referred to the previous contributions (Soga et al., 2016; Li et al., 2018a). In the study, the FEM-LIP



1 method was used to simulate the rockslide, because it overcame the problem of mesh distortion during the large
2 deformation of geomaterials, and could easily take into account the normalized global second order work as a safety
3 factor.

4

5 This paper is organized as follows: section2 presents the engineering geological properties, and the monitoring
6 anchorage force corresponding to the studied rockslide. Section3 describes our FEM-LIP model of the studied
7 rockslide. First, the hydro-elasto-plastic model is briefly presented; second, FEM-LIP modeling of the rockslide is
8 performed; third, the numerical results are analyzed and compared with monitoring data, and the cause of the
9 rockslide is determined. InSection4, some conclusions and future research prospects are discussed.

10

11 **2 Engineering geological properties and real-time monitoring data**

12

13 **2.1 Location of study site**

14

15 The Nanfen open-pit iron mine is one of the largest iron ore mines in Asia, with a mining history of more than 100
16 years. This mine is situated in Nanfen city, Liaoning province, China. In recent years, the local slope has reached 552
17 m (elevation 142 to 694 m, and the bottom elevation of the mining was 160 m in 2011 (Li et al., 2018b)) owing to
18 mining of shallow strata and an increase in mining depth. From 1999 to 2016, several rockslides of different scales
19 were reported, due to both mining activity and rainfall. This study focused on a rockslide on October 31, 2016, which
20 followed excavations on the toe of slope and occurred after a period of rainfall. As shown in Fig. 1, several CRLD
21 cables were installed within the area of an old landslide, to reinforce the slope and monitor the anchorage force, and
22 the studied rockslide at elevations between 442 and 502 m (red zone in Fig. 1) was monitored by the CRLD cable
23 with a number of 478-3. In the same area, a previous rockslide occurred in 2011 at elevations between 442 and 550 m
24 (purple zone in Fig. 1), and it was monitored using the CRLD cable with a number of 478-3' (green point in Fig. 1).

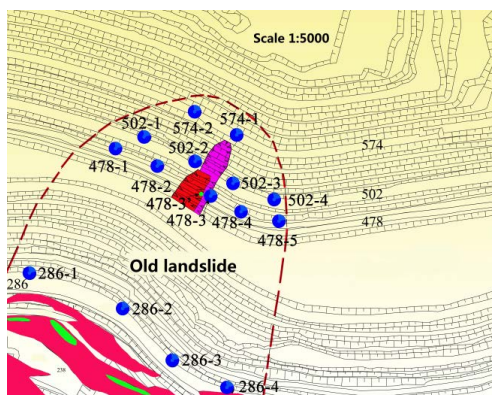
25

26 **2.2 Engineering geological properties**

27

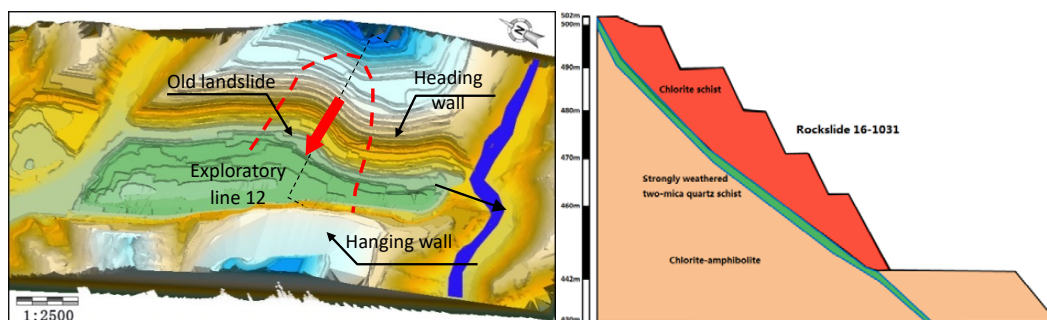
28 The open-pit mine is located at southern side of the Heibeishan inverted anticline, composed of the archaic Anshan
29 group, proterozoic Liaohe group, sinian and quaternary strata. Fig. 2(a) shows that the rockslide occurred on the
30 heading wall, an inclined hard rock slope consisting of chlorite schist and chlorite-hornblende separated by a major
31 weak zone with a slope of 48°, and a strike angle of 295°. The hanging wall is an anti-inclined rock slope consisting
32 principally of migmatitic gneiss and two-mica quartz schist with a hardness of 13–16, and a slope of 46°–48°. The
33 weak zone consisted of the strongly fragmented two-mica quartz schist, with a thickness of about 2m and a length of
34 about 600m (Li et al., 2018b). This weak zone was considered to run through the heading wall, and controlled the
35 stability of the slope on the heading wall. It partially emerged after the rockslide, and was humid and partially
36 sandwiched with mud.

37



1
2
3
4
5
6
7

Figure 1. Plan graph of the Nanfen open-pit iron mine rockslide location. The red area shows the location of the studied landslide that occurred on October 31, 2016. The purple zone shows the boundary of a rockslide that occurred in 2011. Blue circles show the current distribution of force monitoring points, and the green one with a number 478-3' indicates the CRLD cable served during the rockslide in 2011



8
9
10
11

Figure 2. (a) Relief map of the Nanfen mine; (b) geological profile along exploratory line 12

2.3 Site survey and rockslide characteristics

12
13
14
15
16
17
18
19
20
21

In order to understand in detail the geological properties of the open-pit mine, detailed investigations were performed along 28 exploratory lines. For each exploratory line, 140 boreholes were drilled at intervals of 50 m. The dip direction of the studied rockslide was close to the direction of the exploratory line 12 (see Fig. 2); the length along the dip direction was 60 m. The width along the strike line was 50 m, and the corresponding surface was about 3000 m². The rockslide was inclined and had a volume of 1.35×10^4 m³; the maximum thickness of the sliding bodies was about 18 m.

The landslide front was situated on a bench at 442 m elevation, and deposits were concentrated at this level and on the



1 slope between the benches at 442 and 430 m elevation. The trailing edge of the rockslide was situated on the bench at
2 502 m elevation, where a sinking of 7.5m was induced by the rockslide, as shown in Fig. 3.

3
4



5
6
7
8

Figure 3. Sinking observed on the top of the slope



9
10
11

Figure 4. Slip surface consisting of strongly fragmented two-mica quartz schist

12

13 The slip surface mainly included a major geological discontinuity, and was smooth and significantly striated (Fig. 4).
14 The major geological discontinuity, which consisted of strongly fragmented two mica-quartz schist, decreased in
15 strength owing to water infiltration. After the rockslide, rock along the slip surface was moist and the mechanical
16 properties were observed to be significantly degraded. Throughout the rockslide, the slide body did not completely
17 disintegrate, but slid as big blocks along the slip surface.

18

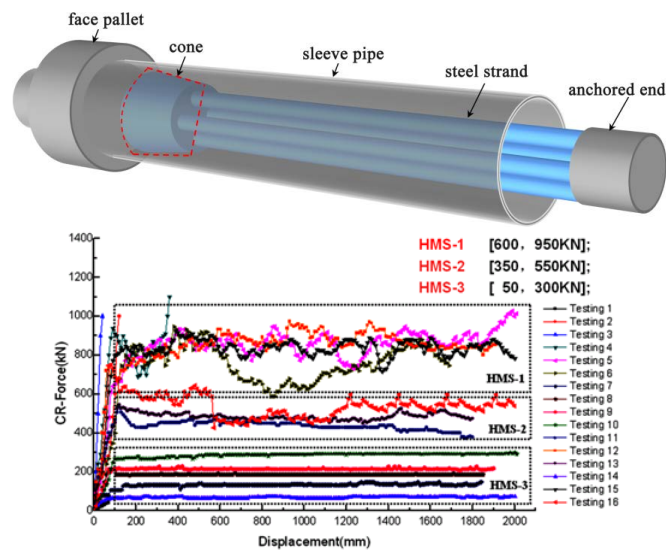
19 **2.4 Real-time monitoring**

20

21 The rock slope was under real-time monitoring by the CRLD cables, developed in the State Key Laboratory for
22 Geomechanics and Deep Underground Engineering. The cable of this type can support large deformation (up to 2 m)



1 while offering constant resistance. The development of the CRLD cable not only reinforced the anchoring ability,
2 but also made it possible to monitor crustal stress in deep strata, and it has successfully predicted the rockslide
3 occurred in 2011, due to the excavation on the toe of the slope (Li et al., 2018b). As shown in Fig.5 (a), the CRLD
4 cable is composed of a piston-like cone body installed on a bundle of cables (6-8 cables), a sleeve pipe with an inner
5 diameter slightly smaller than the diameter of the large-end of the cone; a face pallet served as the retention elements.
6 The anchored end is fixed using grout, and the relative displacement appears between the sleeve pipe and the cables
7 when an axial pull load larger than the constant resistance of the cable is exerted on the face pallet end. The
8 large-end diameter of the cone is slightly larger than the inner diameter of the sleeve pipe, in order to produce
9 sufficient frictional resistance during the relative movement, and to avoid failure of the sleeve pipe. Fig. 5 (b) shows
10 the constant resistance and large deformation properties according to the static pullout tests in laboratory, and this
11 advantage makes the monitoring and prediction possible, during occurrence of landslides, even if the significant
12 relative movement appears on the sliding surface. More details of the CRLD cable and the remote monitoring
13 system can be found in the previous contributions (He, 2009; Sun et al., 2011; He et al., 2014)
14



18 **Figure 5.** (a) Structure of the CRLD cable in three-dimensional view (Li et al., 2018b); (b) constant resistance and
19 large deformation exhibited by the CRLD cable, under static loading.
20

21 In the old landslide area (as shown in Fig. 1), 15 anchorage force monitoring points and two GPS surface
22 displacement monitoring points were installed. One of the surface displacement monitoring points was located on
23 the bench at 478 m, within the domain of the studied rockslide, and it was destroyed by a rockfall during the
24 rockslide (Fig. 6). In the hanging wall, which was stable compared with the footwall, one GPRS relay station and
25 one Beidou satellite relay station were installed. These installations were completed in August 2010 and became



1 operational in October 2010, and have proposed several successful predictions for rockslides occurred in this zone,
2 including the one in 2011 (Li et al., 2018b).

3



4

5

6

Figure 6. GPS surface displacement monitoring point destroyed by rockfall

7

8 2.5 Anchorage force monitoring

9

10 From September 7, 2015 until the rockslide event, the anchorage force monitored at point 478-3 showed a series of
11 slow increases and four sudden increases (Fig. 7a), which increased cumulatively from 320 to 855 kN. The
12 cumulative value never reached the warning threshold proposed by He (2009); therefore, no warning was sent.
13 According to in-situ surveys, no obvious fissures were observed. As a result of constant mining activity, on
14 September 14, 2016 the cumulative increase of anchorage force exceeded 300 kN. Although no fissures were
15 observed, the first long-term warning was sent due to the sudden increase, and the monitoring frequency was
16 increased to twice per hour. After September 14, 2016, the anchorage force at this point remained constant until a
17 sudden increase on October 30, 2016 (Fig. 7b), when the cumulative force increase exceeded 580 kN and a few
18 surface fissures appeared. Mining activities were stopped, and a medium-term warning was sent. In the following
19 days, the curve remained constant and no obvious fissures continued to develop; therefore, mining excavations
20 restarted along the bench at 442 m elevation on October 28, 2016. On October 30, the curve of anchorage force
21 suddenly increased again before decreasing abruptly at 8:56 on October 31 (Fig. 7b), after a period of rainfall. A
22 short-term warning was sent and all staff was evacuated. At 23:52 on October 31, the rockslide occurred, prompting
23 a large volume of rock to slide downhill and pile up on the bench at 442 m elevation.

24

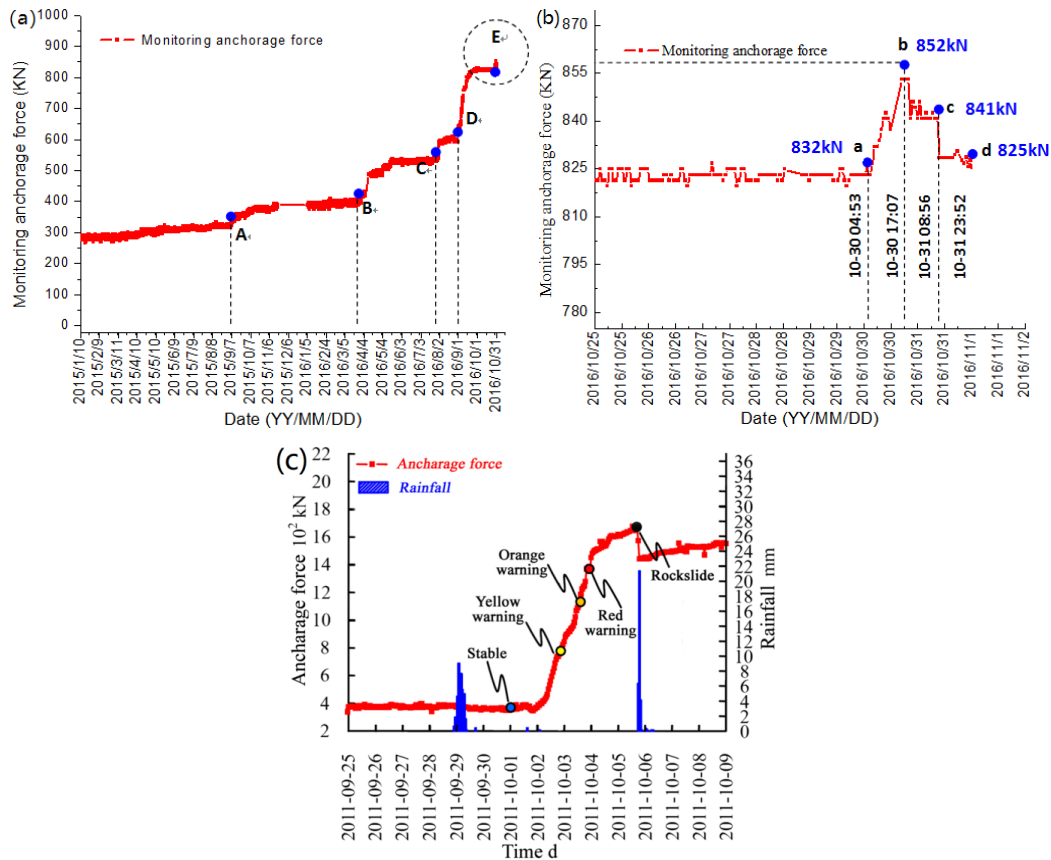
25 Mining activities on the toe of the rock slope explain the four sudden increases in monitored anchorage force.
26 However, the last excavation before the rockslide occurred on October 28, 2016, and there was no obvious increase
27 in the curve of anchorage force (Fig. 7b), though it remained a high level. On October 30, 2016, the last abrupt
28 increase in anchorage force appeared during a period of intense rainfall, before the subsequent rockslide on October
29 31, 2016. Based on the survey data, this rainfall was considered to be the cause of the rockslide.

30



1 Fig. 7 (c) shows the monitoring anchorage force during the excavation-induced rockslide in 2011, and a similar
 2 evolution is observed. Comparing Figs. 7 (a) and (b), both of the peak and the decrease during the rockslide are in a
 3 significantly larger scale, with values of 1678 kN and about 200 kN, respectively. The reason was that the CRLD
 4 cable 478-3' was located within the range of the rockslide 2011, and thus completely reflected the variation of the
 5 sliding force; the CRLD cable 478-3 was located outside the range of the rockslide 2016, so the variation of the
 6 sliding force was partially reflected. However, it does not obstruct the successful monitoring and prediction.
 7

8



9

10 **Figure 7.** Real-time monitoring curve of the anchorage force. (a) points A–E represent five sudden increases before
 11 the rockslide in 2016; (b) anchorage force during the rockslide in 2016 (partially enlarged from part a); (c)
 12 monitoring anchorage force during the rockslide in 2011 (Li et al., 2018b).
 13

14 The prediction of geological disasters is a complex issue, with rainfall, earthquakes, and human activities all
 15 presenting potential triggers. Variables such as stress, strain, and water pressure are often used for monitoring
 16 purposes; however, for landslides, these variables are not always predictive. Anchorage force monitoring was
 17 chosen because it can accurately reflect increasing sliding force and the degradation of the mechanical properties of



1 geomaterials, which in turn result in increased anchorage force and the possibility of slope instability. Furthermore,
2 this method remains useful in cases where the slope becomes unstable and the anchorage force increases, but
3 displacement on the slope surface does not change, or measurement on the slope surface cannot work.

4

5 **3 Numerical analysis using FEM-LIP**

6

7 Different instability mechanisms complicate the analysis of rockslides, and many issues remain open to discussion.
8 Although the stability of rock slopes hinges on a large number of factors, such as the type and the history of the rock,
9 the size of the slope and so on, the geological discontinuities, which have lower strength and more commonly
10 developed fissures, also play an important role in the mechanical behavior and the stability, especially for the
11 geological discontinuity controlled slopes (Regmi et al., 2012; Zhang et al., 2016). Generally, geological
12 discontinuities have higher porosity and function as channel systems for water infiltration (Regmi et al., 2012). The
13 rock slope in the study area is characterized by a major geological discontinuity of highly fragmented two-mica
14 quartz schist. The two-mica quartz schist is highly fragmented presenting as blocks and debris, and filled with mud,
15 and can be considered as granular material.

16

17 We used the FEM-LIP method to realize the large deformation during the rockslide. By using the FEM-LIP method,
18 the simulated materials are discretized by an Eulerian mesh and a series of Lagrangian material points, the control
19 equations are solved and the solution is obtained in the Eulerian calculation mesh. After interpolation according to
20 corresponding shape functions, the internal variables (stress, strain, water content, etc.) can be obtained for each
21 material point. At each time step, the position of material points is refreshed. In this process, the material points
22 move in line with the deformation of the studied material, but the mesh is not deformed. The relative movement
23 between the material points and the mesh makes the simulation of large deformation possible.

24

25 **3.1 Elasto-plastic model incorporating complete hydro-mechanical coupling**

26

27 In this study, an elasto-plastic model, the PLASOL model, was used to describe the elasto-plastic behavior with
28 plastic hardening for the major discontinuity, according to experimental data (as shown in Figs. 9). For describing the
29 decrease of strength on the major geological discontinuity due to wetting, a Bishop's type effective stress formulation
30 and modified Van Genuchten water retention curves (WRCs) were introduced into the PLASOL model.

31

32 *3.1.1 PLASOL model*

33 This non-associated elasto-plastic model was first used for solving structural geology problems within the
34 framework of finite element methods (Barnichon, 1998), and is also appropriate for dealing with a wide range of
35 geomaterials (Lignon et al., 2009; Prime et al., 2013; Prunier et al., 2016; Li et al., 2016; Li et al., 2018b). A Van
36 Eekelen plasticity criterion (Van Eekelen, 1980), which is similar to the Mohr-Coulomb criterion but avoids
37 geometric singularities, is used as the plastic limit in the model. Let us invoke three effective stress vector invariants



1 $J_{1\sigma'} = \text{tr}(\sigma')$, $J_{2\sigma} = \sqrt{\text{tr}(\tau^2)}$, $J_{3\sigma} = \sqrt[3]{\text{tr}(\tau^3)}$, ($\tau = \sigma' - \frac{1}{3}\text{tr}(\sigma')I$), where σ' is the Bishop's effective stress,
 2 calculated as follows:

$$3 \quad 4 \quad \sigma' = \sigma - u_a \mathbf{m} + \chi(u_a - u_w) \mathbf{m} \quad (1)$$

5
 6 where σ , u_a , and u_w are the total stress vector, the isotropic air pressure, and the isotropic water pressure,
 7 respectively; χ is the Bishop's parameter taken as a scalar in this model; and $\mathbf{m}^T = (1,1,1,0,0,0)$, $s = u_a - u_w$ is
 8 the suction value. For the sake of simplification, the Bishop's proposition (Bishop, 1959) was used to formulate
 9 parameter χ in this study:

$$10 \quad 11 \quad \chi = Sr \quad (2)$$

12
 13 Considering the Bishop's effective stress, the expression of the Van Eekelen yield criterion can be written as
 14 follows:

$$15 \quad 16 \quad f = J_{2\sigma} + m \left(J_{1\sigma'} - \frac{3c}{\tan\varphi_c} \right) = 0 \quad (3)$$

17 where c is cohesion, φ_c is the mobilized friction angle under triaxial compression conditions, and m is a coefficient
 18 defined as follows:

$$19 \quad 20 \quad m = a(1 + b \sin(3\beta))^n \quad (4)$$

21
 22 The Lode angle β is given by $\cos 3\beta = \sqrt{6} \left(\frac{J_{3\sigma}}{J_{2\sigma}} \right)^3$, parameters a and b are functions of the friction angles φ_c
 23 (compression path) and φ_e (extension path), as defined by:

$$24 \quad 25 \quad a = \frac{r_c}{(1+b)^n}, \quad b = \frac{\left(\frac{r_c}{r_e}\right)^{\frac{1}{n}} - 1}{\left(\frac{r_c}{r_e}\right)^{\frac{1}{n}} + 1}$$

26 (5)

27
 28 where parameters r_c and r_e are the reduced radii for triaxial compression and extension tests, respectively, and are
 29 calculated as follows:

$$30 \quad 31 \quad r_c = \frac{1}{\sqrt{3}} \left(\frac{2 - \sin\varphi_c}{3 - \sin\varphi_c} \right), \quad r_e = \frac{1}{\sqrt{3}} \left(\frac{2 \sin\varphi_e}{3 + \sin\varphi_e} \right) \quad (6)$$

32
 33 The exponent n controls the shape of the yield surface, and the default value is -0.299 according to the work of Van
 34 Eekelen (1980).



1

2 In the PLASOL constitutive model, the plastic hardening of the yield surface during loading is controlled by internal
 3 variables (the cohesions and friction angles), which are functions of the Von Mises equivalent plastic strain: $\boldsymbol{\varepsilon}_{eq}^p =$
 4 $\sqrt{\frac{2}{3}e_{ij}^pe_{ij}^p}$, ($\boldsymbol{e}^p = \boldsymbol{\varepsilon}^p - \frac{1}{3}\text{tr}(\boldsymbol{\varepsilon}^p)\boldsymbol{I}$). Consequently, the compression, extension friction angles, and cohesion formulated in
 5 Equations (7), vary between elastic initial values ($c_0, \varphi_{e0}, \varphi_{c0}$) and plastic limit values ($c_f, \varphi_{ef}, \varphi_{cf}$), depending
 6 on the equivalent plastic strain $\boldsymbol{\varepsilon}_{eq}^p$ and the hardening parameters B_c and B_p (Lignon et al., 2009; Prunier et al.,
 7 2009).

8

$$\begin{aligned} \varphi_c &= \varphi_{c0} + \frac{(\varphi_{cf} - \varphi_{c0})\boldsymbol{E}_{eq}^p}{B_p + \boldsymbol{E}_{eq}^p} \\ \varphi_e &= \varphi_{e0} + \frac{(\varphi_{ef} - \varphi_{e0})\boldsymbol{E}_{eq}^p}{B_p + \boldsymbol{E}_{eq}^p} \\ c &= c_0 + \frac{(c_f - c_0)\boldsymbol{E}_{eq}^p}{B_c + \boldsymbol{E}_{eq}^p} \end{aligned} \quad (7)$$

9

10 Furthermore, the dilatation angle ψ is required to define the non-associated plastic law (Prunier et al., 2009; Li et al.,
 11 2016). In total, 13 parameters are required to adequately describe the elasto-plastic behavior of geomaterials:

12

- 13 E, ν : Young's modulus and Poisson's coefficient, respectively
- 14 $\varphi_{c0}, \varphi_{cf}$: mobilized friction angles at elastic and plastic limits under triaxial compression, respectively
- 15 $\varphi_{e0}, \varphi_{ef}$: mobilized friction angles at elastic and plastic limits under triaxial extension, respectively
- 16 ψ_c, ψ_e : dilatation angles under triaxial compression and extension, respectively
- 17 c_0, c_f : cohesion at elastic and plastic limits, respectively
- 18 B_c, B_p : hardening parameters
- 19 n : exponent controlling yield surface shape

20

21 3.1.2 Water retention curves

22 In order to determine the Bishop's parameter χ from the degree of saturation, it is necessary to determine the
 23 relationship between suction and the degree of saturation. A large number of water retention models have been
 24 proposed (Van Genuchten, 1980; Parlange, 1980; James et al., 1998; Feng and Fredlund, 1999), and the modified
 25 Van Genuchten model (Van Genuchten, 1980; James et al., 1998) was selected to complete the hydro-mechanical
 26 coupling in this study because the boundary curves are simple and commonly used. The formulation of this model is
 27 as follows:

28

$$S r_v = S r_{res} + (S r_{sat} - S r_{res}) \left(1 + \left(\frac{a_{ps}}{P_{atm}} \right)^{n_v} \right)^{\frac{1}{n_v} - 1} \quad (8)$$

29



1

2 where index v stands for d or w in the drying or wetting processes, respectively; Sr_{res} , Sr_{sat} , and Sr_v are the
 3 residual, saturated, and current degrees of saturation, respectively; and a_v and n_v are two parameters depending
 4 on porosity, whose expressions can be found in (Arairo et al., 2013).

5

6 3.1.3 Second order work criterion

7 In this study, instead of classical plasticity criteria, the second order work criterion was used, and the sign of the
 8 second order work indicated local and global failures.

9

10 As the lower border of the bifurcation domain and the most conservative failure criterion, the second order work
 11 criterion has been systematically investigated for evaluating the stability and failure of geomaterials (soils and
 12 jointed rocks) (Darve and Servant, 2004; Darve et al., 2004; Laouafa et al., 2011; Duriez et al., 2011; Nicot et al.,
 13 2011). The local second order work and its normalized form are written as follows:

14

$$15 \quad d^2w = d\sigma'_{ij}d\varepsilon_{ij} \quad (9a)$$

$$16 \quad d^2w_{norm} = \frac{d^2w^i}{\|d\sigma'^t\|\|d\varepsilon^t\|} = \cos\alpha^i$$

17 (9b)

18

19 where d^2w_{norm} is the normalized local second order work at material point i , and $\|d\sigma'^t\|$ and $\|d\varepsilon^t\|$ are the
 20 norms of the stress increment and the strain increment of the material point i , respectively. Hence, the d^2w_{norm} is
 21 equal to the cosine of the angle α between the incremental stress and strain vectors, and its value is thus limited
 22 between -1 and 1 . If $d^2w_{norm} > 0$ for all loading directions, the material is strictly stable; if $d^2w_{norm} < 0$ at
 23 least in one loading direction, the material is considered potentially unstable; and if $d^2w_{norm} < 0$ in the current
 24 loading direction, the material is unstable, and diffuse or localized failures can occur. In order to save
 25 computational time in the simulation, the local second-order work (see Equations 9) was only calculated for the
 26 current loading direction.

27

28 In order to analyze the global instability for the boundary value problems, an appropriate expression of normalized
 29 global second order work is needed. According to the integral expression of d^2w (Hill, 1958): $D^2W =$
 30 $\int_V d\sigma' d\varepsilon dV = dQ^t dF$, with V the volume of interest, dQ and dF the global nodal incremental displacement and
 31 force, respectively, the normalized global second order work was firstly proposed as follows (Khoa et al., 2006):

32

$$33 \quad D^2W_{norm} = \frac{D^2W}{\|dQ\|\|dF\|} = \frac{dQ^t dF}{\|dQ\|\|dF\|} = \frac{\sum(d^2w^i \cdot \omega^i j^i)}{(\sum \omega^i j^i)(\sum \|d\sigma'^t\|\|d\varepsilon^t\|)}$$

34 (10)

35



1 where ω^i is the numerical weight of the material point i , and J^i is the determinant of the Jacobian matrix. This
2 expression is convenient to compute, but it is mesh dependent (Prunier et al., 2009). Recently, a new expression,
3 independent from the number of elements, has been proposed as follows (Prunier et al., 2016):

4

$$5 \quad D^2 W_{norm} = \frac{D^2 W}{\int_V \|d\sigma\| \|d\varepsilon\| dV} = \frac{\sum(d^2 w^i \cdot \omega^i J^i)}{\sum(\omega^i J^i \|d\sigma^i\| \|d\varepsilon^i\|)} \quad (11)$$

6

7 Evidently, both the numerators in equations 10 and 11 are identical, but the denominator in equation 10 is larger
8 with finer mesh, and that in equation 11 is mesh independent. Noted that equation 11 needs the use of a sufficiently
9 open numerical code, in order to manipulate basic integration operators over the elements or to get access to shape
10 functions and mesh description.

11

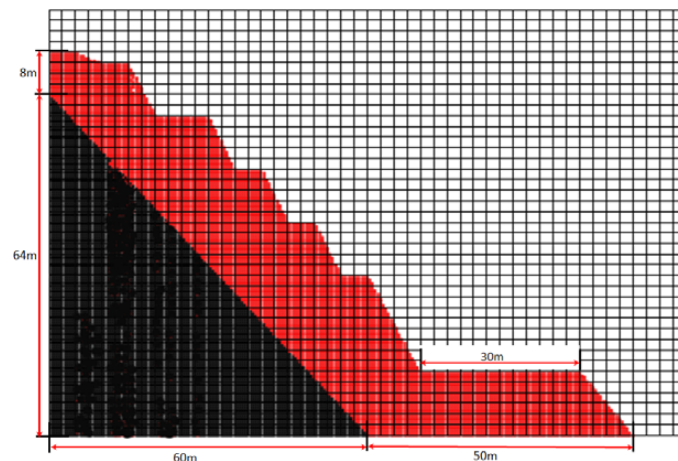
12 **3.2 Numerical analysis of the Nanfen rockslide**

13

14 *3.2.1 Geometry and boundary conditions of the rockslide model*

15 Geological data from the field survey and engineering geology drilling showed that the sliding surface was principally
16 along the major geological discontinuity (i.e., along strongly fragmented two-mica quartz schist). The FEM-LIP model
17 of the rock slope was established in a calculation domain, in which the horizontal and vertical dimensions were 120 m
18 and 80 m, respectively. The calculation domain was discretized by 1920 meshes, and each mesh consisted of 25
19 material points. The slope was composed of three materials (Fig. 8): chlorite-hornblende stable bedrock, chlorite
20 schist slide bodies, and a two-mica quartz schist as the major geological discontinuity. The model dimensions were as
21 follows: height 72 m; width 110 m; bedrock height and width 64 and 60 m, respectively; widths of the seven benches
22 were 5, 5, 10, 5, 5, 5, and 30m, respectively.

23



24

25

26 **Figure 8.** Geometry of the rock slope FEM-LIP model. Stable bedrock (black layer) is chlorite-hornblende. The slide



1 body (red) comprises chlorite schist. The interface between the black and red layers comprises a two-mica quartz
2 schist functioning as the major geological discontinuity

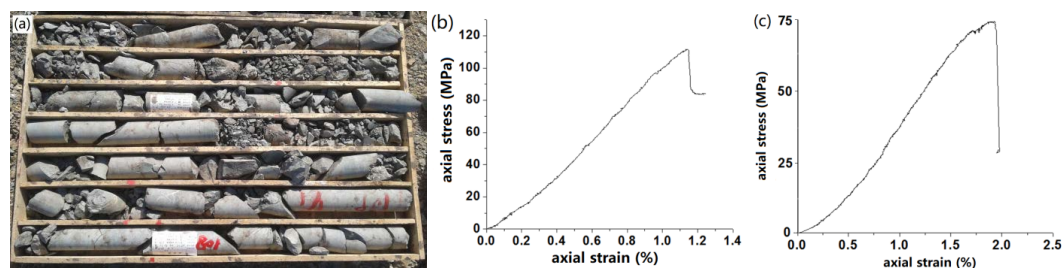
3
4 In this model, all boundaries were free slip, and the horizontal displacement at the left boundary and the vertical
5 displacement at the bottom boundary were constrained. Gravity increased linearly for the first 150 time steps, until a
6 value of 9.81 m/s^2 was reached. For sake of simplification, the initial suction in the major geological discontinuity
7 was assumed homogeneously distributed. Moreover, an excavation on the toe of the slope was performed at the 38th
8 hour, and rainfall on the top surface induced downward water infiltration under a constant water flux of 24 mm/h over
9 21 hours.

10

11 3.2.2 Determination of physical parameters

12 In the model, all three materials were described by elasto-plastic constitutive law, and the hydro-mechanical
13 coupling was taken into account only for the chlorite schist and the highly fragmented two-mica quartz schist. The
14 geomechanical parameters were estimated according to the triaxial compression tests and geological survey. The
15 sample of two mica-quartz schist for the triaxial compression tests are showed in Fig. 9 (a). Figs. 9 (b) and (c) gave
16 typical stress-strain curves under a confining stress of 20 MPa, for the sample with a degree of saturation of 43%
17 and the one in saturated state, respectively. The values of c_0 and c_f could be thus estimated. It was necessary to
18 reduce the strengths obtained from the experimental data, because the weak zone emerged after the rockslide
19 presented a high discontinuity density. According to the empirical strength reduction method, the cohesions used in
20 the paper were reduced by Equation $c = \frac{c_i}{n+k}$. c and c_i were reduced cohesion and that of intact rock sample,
21 respectively. n was discontinuity density, which was assigned to be 30, and k was a coefficient related to the
22 fragmentation index with a value of 40. Considering the empirical strength reduction method and the values
23 recommended by in-situ tests (Sun et al., 2011; Yang et al., 2012; Li et al., 2018), the elasto-plastic parameters were
24 summarized in Table 1.

25



26

27

28 **Figure 9.** Triaxial compression tests for determining the geomechanical parameters of the two mica-quartz schist. (a)

29 samples for the experimental tests, typical stress-strain relations under confining stress of 20 MPa, for (b) the

30 samples with a degree of saturation of 43%, and (c) the samples in the saturated state respectively.

31

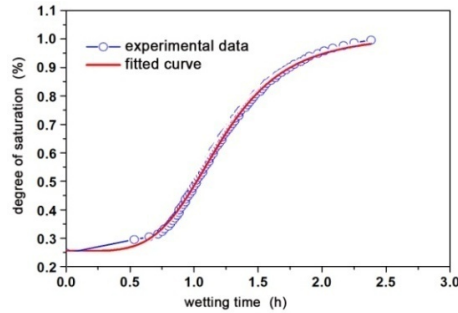


Figure 10. Wetting test for the strongly fragmented two mica-quartz schist sample

The degree of saturation of the two-mica quartz schist before rainfall was 43%. The permeability of the two-mica quartz schist was $k_1 = 2 \times 10^{-1}$ cm/s and that of the chlorite schist was $k_2 = 1 \times 10^{-8}$ cm/s, according to a top surface aperture of 1 mm and a slope surface aperture of less than 0.025 mm; consequently, the permeabilities were considered strong and very weak, respectively (GB50487-2008). It should be noted that decreasing strength of rocks under rainfall conditions is generally due to the saturation effect in the unsaturated stage and the softening effect in the saturated stage. The latter is generally a long-duration process, and is not the objective of this study. The former results in an increasing degree of saturation and a decreasing suction; thus, the apparent cohesion and strength are reduced according to Equation 12:

$$\tau = c' + \sigma' \tan \varphi' = (c' + \chi \sigma \tan \varphi') + \bar{\sigma} \tan \varphi' \quad (12)$$

where c' is the effective cohesion measured from the sample on the top surface after rainfall, and $c = c' + \chi \sigma \tan \varphi'$ is the apparent cohesion measured from the sample before the rockslide. With the assumption of $\chi = S_r$, the suction after rainfall could be considered 0, and the initial suction before rainfall could be obtained by the expression: $c - c' = \chi \sigma \tan \varphi' = 23 \text{ kPa}$. The initial suction was thus 105 kPa.

According to the wetting test (Fig. 10), $S_{r_{sat}} = 1$ and $S_{r_{res}} = 0.27$. The hydraulic parameters could be simplified as $a_d = a_w$ and $n_d = n_w$, because the water infiltration could be simplified as a monotonous wetting process. With the initial and final degree of saturation and the suction, the parameters could be back-calculated (Table 2).

Table 1: Elasto-plastic parameters

Properties	E	ν	φ_{c0} $= \varphi_{e0}$ (°)	φ_{cf} $= \varphi_{ef}$ (°)	c_0 (kPa)	c_f (kPa)	c_0' (kPa)	c_f' (kPa)	ψ_c $= \psi_e$ (°)	B_p	B_c	ρ (Kg/ m^3)
Chlorite-hornblend e	36	0.31	41	41	414	414	-	-	1	0.01	0.02	2910
Chlorite schist	25	0.28	36	38	71	77.4	-	-	1	0.01	0.02	1825



Two-mica quartz schist	0.8	0.26	24	27	64	69	42	46	1	0.01	0.02	1675
------------------------	-----	------	----	----	----	----	----	----	---	------	------	------

1

2 **Table 2: Hydraulic parameters of two-mica quartz schist and chlorite schist**

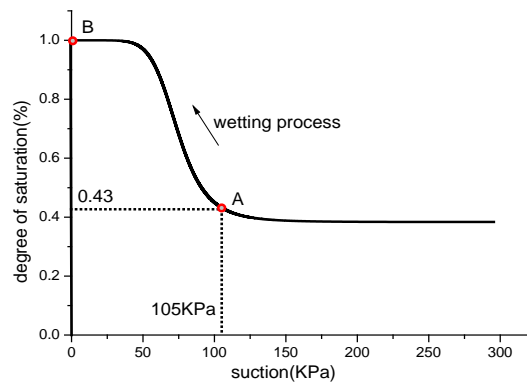
a_d	n_d	a_w	n_w	Sr_{sat}	Sr_{res}
1.94	3.03	1.94	3.03	1	0.27

3

4 *3.2.3 Results and analysis*

5

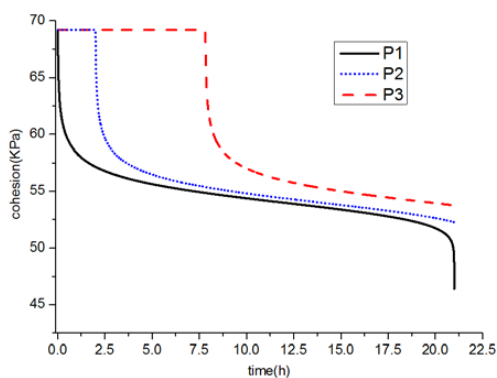
6 Fig. 11 shows the suction-degree of saturation curve for the monotonous wetting process. The segment from point A
 7 to point B corresponds to the two mica-quartz schist. At point A, the suction was 105 kPa, corresponding to a degree
 8 of saturation of 43%. At point B, the suction was 0, corresponding to a degree of saturation of 100%. For a detailed
 9 comparison of apparent cohesion and second order work at different positions along the slope, three material points,
 10 P1, P2, and P3, were selected on the top surface, the middle of the slope, and the toe of the slope, respectively (Fig.
 11 13a). The decrease of apparent cohesion was induced by the decrease in suction, according to Equation 12. Clearly,
 12 the material at point P1 underwent an immediate decrease of apparent cohesion from 69 to 46 kPa, and points P2
 13 and P3 showed a delay in strength reduction (Fig. 12) because of infiltration at different altitudes; therefore, the
 14 homogeneous initial suction began to decrease at different times.



15

16 **Figure 11.** Relationship between suction and degree of saturation during the monotonous wetting process. The
 17 segment from point A to point B shows the two mica-quartz schist

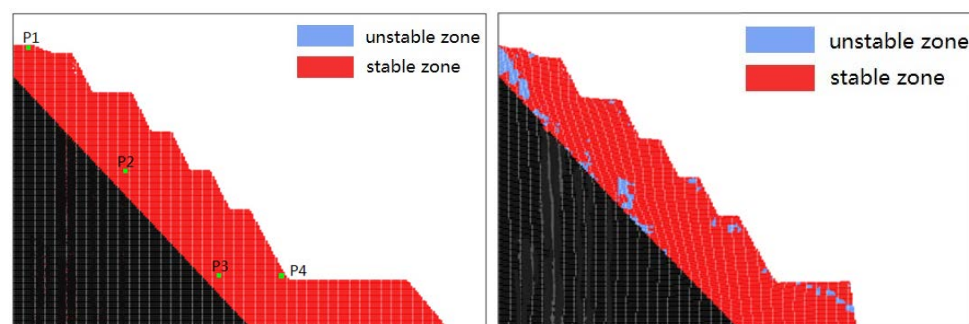
18



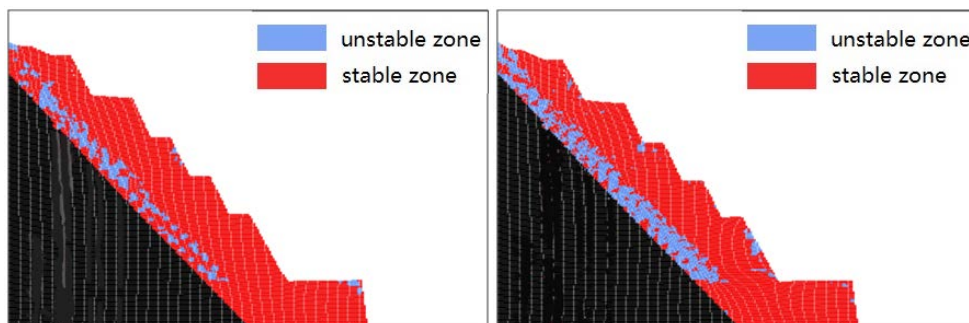
1
2
3

Figure 12. Evolution of apparent cohesion at points P1, P2, and P3

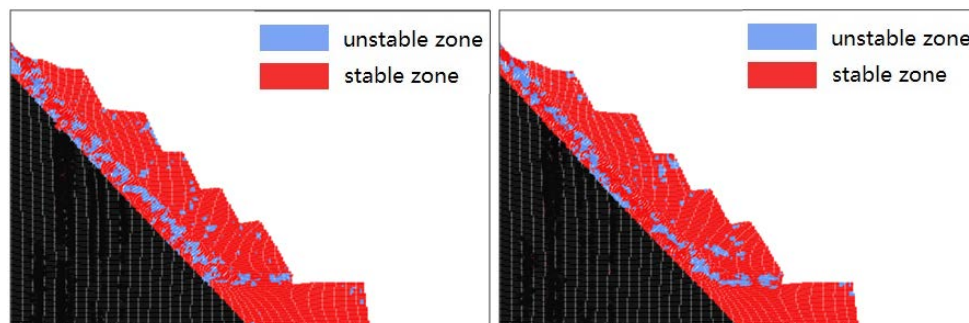
4

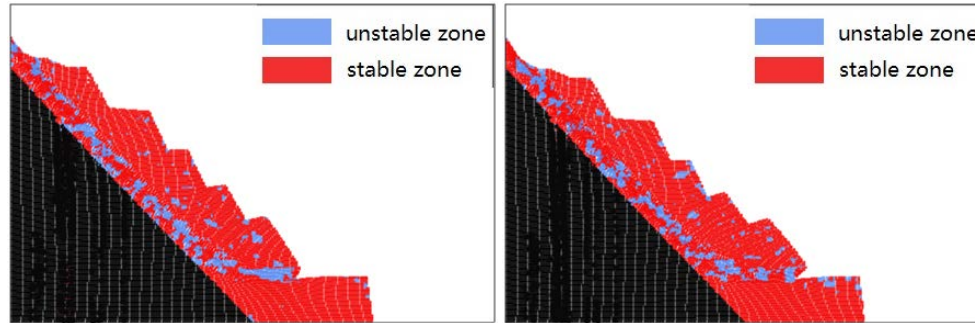


5



6



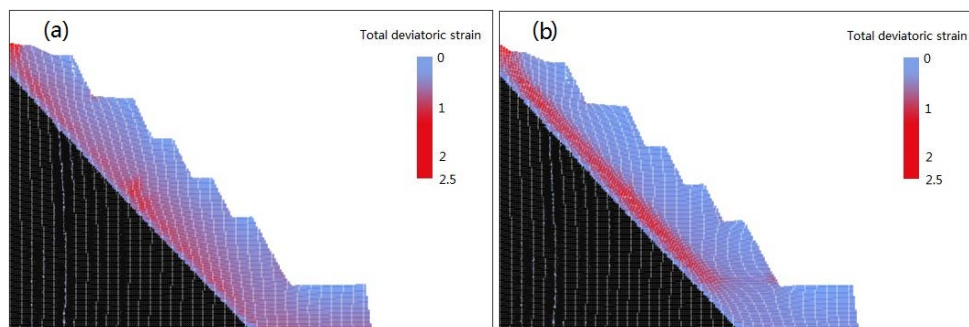


1
2
3
4
5
6
7

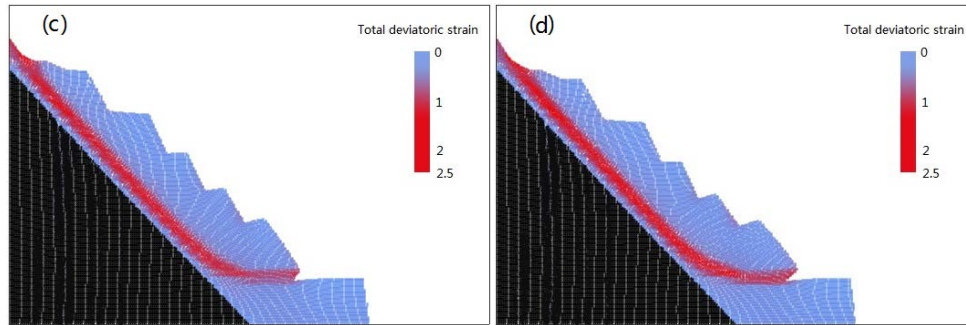
Figure 13. Stable zones (red) and the development of unstable zones (blue) during the consistent evolution of the rockslide. (a) Initial configuration after gravity initialization; (b) unstable zones after excavation; (c) water infiltration after 12 h; (d) Water infiltration after 25 h, $D^2W_{norm} = 0$; (e) slip configuration after 1s; (f) slip configuration after 3s; (g) Slip configuration after 5s; (h) Slip configuration after 7s

8 Fig. 13 shows the development of unstable zones under excavation and water infiltration conditions, and the entire
 9 rockslide process at various elapsed times. The unstable zones correlate to a negative local second order work
 10 calculated by Equation 9a. Unstable zones first concentrate at material points on the top and toe of the slope,
 11 because of excavation at the toe (Fig. 13b). Compared with Fig.15, d^2w_{norm} at points P1 and P2 indicates a slight
 12 decrease, and point P3 shows a more significant decrease at 38 h, when excavation on the toe was performed.
 13 However, this change did not induce any clear instability, and all three material points remained stable. During the
 14 subsequent 46 hours after excavation, values of d^2w_{norm} remained positive and constant, and that of point P3
 15 progressively increased. When water infiltration occurred on the top surface, the d^2w_{norm} of points P1, P2, and P3
 16 started to decrease quickly, and became zero at 92.8 h, 102 h, and 109 h, respectively, according to Fig.15, which
 17 signifies failures at these points. Figs. 13 (c and d) also shows that unstable zones developed quickly along the major
 18 geological discontinuity under infiltration conditions, but few unstable zones appeared in the upper slide bodies
 19 because of the very low permeability ($k_2 = 1 \times 10^{-8}$ cm/s).

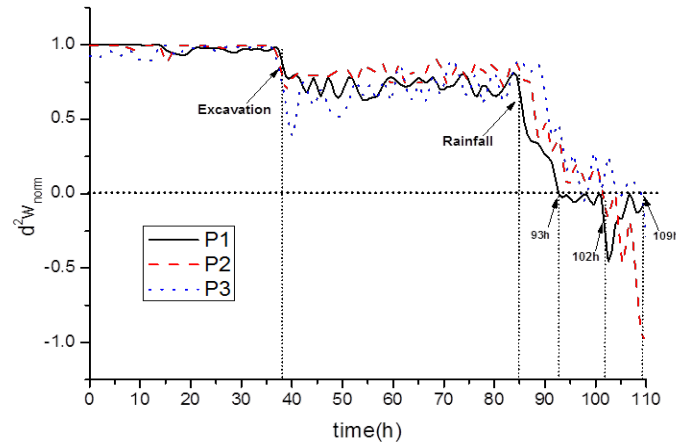
20



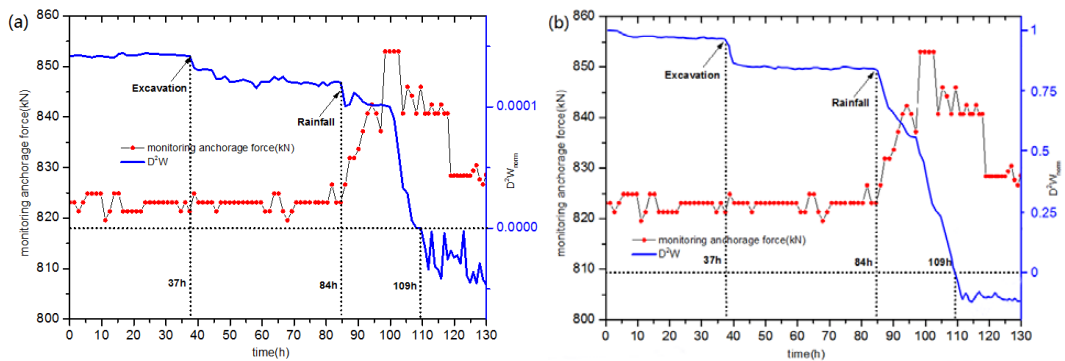
21



1
 2 **Figure 14.** Evolution of the shear strain band: (a) after excavation; (b) global failure, $D^2W_{norm} = 0$; (c) slip
 3 configuration after 5s; and (d) slip configuration after 7s



4
 5 **Figure 15.** Evolution of normalized local second order work with time
 6



7
 8 **Figure 16.** Evolution of monitoring anchorage force and normalized global second order work, computed according to
 9 (a) equation (10); and (b) equation (11)



1

2 After failure, the simulated rockslide involved continuous, large deformation (Figs. 13e-h). The shear strain band
3 developed first along the major discontinuity, and then a horizontal band appeared between that and the toe of the
4 slope (Fig. 14). The shear strain band became well developed and failure occurred. Clearly, the rockslide developed
5 owing to large deformation along the major discontinuity and at the toe of the slope. Most zones of the upper
6 chlorite schist remained stable during the elastic stage, and then slipped as one mass along the two-mica quartz
7 schist weak zone. The simulation results were therefore consistent with the real case.

8

9 Figs. 16 illustrates the evolution of the normalized global second order work calculated according to equations (10)
10 and (11), respectively, and compares them with that of the monitored anchorage force. The excavation at 37 h
11 evoked a slight decrease in D^2W_{norm} , correlated with the trend in d^2w_{norm} . However, themining activity on the toe
12 of the slope did not influence significantly the stability of the slope, and the curve of anchorage force only showed a
13 slight fluctuation before returning quickly to its previous value. The second significant decrease of D^2W_{norm} was
14 caused by water infiltration at 84–105 h. During the rainfall, D^2W_{norm} decreased quickly with failure along the
15 major discontinuity, and became zero at 109 h, after 4 h of rainfall. At the same time, the anchorage force reached a
16 peak of 852 kN, because the decreasing apparent cohesion was not sufficient to resist the increasing sliding force. The
17 anchorage force then decreased to 841 kN, corresponding to a local slide between the benches at 502 and 490 m
18 elevation. Subsequently, the anchorage force showed a second decrease, to a value of 825 kN, at the point of global
19 failure and the rockslide event. The trend of D^2W_{norm} mainly correlates to that of the monitoring data, and both
20 prove that the October 31, 2016 rockslide was induced by rainfall. Regarding the comparison between the two global
21 second order work, both of them presented two sudden decreases during excavation and rainfall were exerted, and
22 both of them vanished at 109 h. It was evident that their evolutions were mainly similar, because the numerators in
23 equations (10) and (11) were identical. However, the value of the former decreased with the finer mesh, that of the
24 later varied between 1 and 0 in any case, and presented less fluctuation. The normalized global second order work
25 computed by equation (11) can theoretically be used as a safety factor for analyzing the global stability of a
26 boundary value problem.

27

28 **4 Conclusions**

29

30 In this study, we considered a recent rockslide in the Nanfen open-pit iron ore mine that was successfully predicted
31 using the real-time monitoring system. The core of the monitoring system was the CRLD cable, whose properties,
32 the constant resistance and large deformation, made the disaster prediction possible, during the occurrence of
33 landslides. The CRLD cable can monitor and reflect increasing sliding force and the degradation of the mechanical
34 properties of geomaterials in deep strata, despite of the triggering factors, and the successful predictions of the
35 excavation-induced rockslide in 2011 and the rainfall-induced rockslide in 2016 are good evidences. This
36 monitoring system has exhibited its reliability and generality, and further generalization is thus expected.

37



1 Based on in-situ surveys and monitoring data, this rockslide was considered to have been induced by rainfall.
2 Mining activities augmented the instability risk but were not the direct cause of the rockslide. A numerical analysis
3 was performed using the FEMLIP method. An elasto-plastic constitutive model incorporating hydro-mechanical
4 coupling and the second order work criterion was employed in order to solve water infiltration and instability
5 problems. The results were carefully analyzed, comparing with the monitoring data, and several conclusions could
6 be obtained:

7

8 1. The evolution of second order work indicated a good correlation with monitoring data, both for the failure
9 mechanism predicted by the local values of second order work and failure time by its global value. Water infiltration
10 induced a decrease in strength of the major geological discontinuity, and a subsequent increase in the anchorage
11 force to support the increasing sliding force due to adjacent sliding bodies. Accordingly, the decrease in the local
12 and global values of second order work was a response to the decreasing geomaterial strength. Finally, water
13 infiltration along the major geological discontinuity prompted the rockslide.

14 2. Both of the Equations (10) and (11) of the normalized global second order work were implanted in FEMLIP code,
15 and the corresponding results were compared. Equation (11) resulted in a result with less fluctuation, and limited
16 within the range 0 to 1, despite of the mesh. It can be used as a safety factor, more general and more physical than
17 the numerical divergence of the calculation.

18 3. Differing from the classical method, such as the FDM method, the complete evolution of the rockslide could be
19 simulated in a unified frame using the FEMLIP method, which has been shown more generally as useful for
20 predicting the disaster domain and evaluating the dynamic effect on the retaining wall. The numerical analysis is a
21 good assistant tool for understanding the failure mechanism and predicting landslides.

22

23 This research suggests that subsequent mining activities should be undertaken with more care, and geological
24 discontinuities with low strength and high permeability should be avoided as much as possible. Geological surveys
25 and monitoring measures should also be carefully consulted. These results have to be compared with some adequate
26 numerical models to fully understand both the failure mechanisms and the critical parameter values inducing the
27 catastrophic instability.

28

29

30

31

32

33

34

35

36



1 **References**

2

3 Abe, K., Soga, K., and Bandara, S.: Material point method for coupled hydromechanical problems, *Journal of*
4 *Geotechnical and Geoenvironmental Engineering*, 140(3), 04013033, 2013.

5 Arairol, W., Prunier, F., Djéran-Maigre, I., and Darve, F.: A new insight into modeling the behavior of unsaturated
6 soils. *International Journal for Numerical and Analytical Methods in Geomechanics*, 37(16), 2629-2654, 2013.

7 Bandara, S., Ferrari, A., and Laloui, L.: Modelling landslides in unsaturated slopes subjected to rainfall infiltration
8 using material point method, *International Journal for Numerical and Analytical Methods in Geomechanics*, 40(9),
9 1358-1380, 2016.

10 Barnichon, J.D.: Finite element modelling in structural and petroleum geology, Ph.D. Thesis, University of Liege,
11 1998.

12 Bishop, A.W.: Principle of effective stress, *Teknisk Ukeblad*, 106(39), 859-863, 1959.

13 Cascini, L., Cuomo, S., Pastor, M., Sorbino, G., and Piciullo, L.: SPH run-out modeling of channelized landslides of
14 the flow type, *Geomorphology*, 214(2), 502-513, 2014.

15 Chen, H., Dadson, S., and Cui, Y.: Recent rainfall-induced landslides and debris flow in northern Taiwan,
16 *Geomorphology*, 77(1-2), 112-125, 2006.

17 Cuomo, S., Prime, N., Iannone, A., Dufour, F., Cascini, L., and Darve, F.: Large deformation FEM-LIP drained
18 analysis of a vertical cut, *Acta Geotechnica*, 8(2), 125-136, 2013.

19 Darve, F. and Servant, G.: Fundamental of constitutive equations for geomaterials, *Degradations and instabilities in*
20 *geomaterials*, Springer Vienna, 461, 1-33, 2004.

21 Darve, F., Servant, G., Laouafa, F., and Khoa, H.D.V.: Failure in geomaterials : continuous and discrete analyses,
22 *Computer Methods in Applied Mechanics and Engineering*, 193(27-29), 3057-3085, 2004.

23 Dong, H.K., Ivan, G., and Arumugam, B.: Back analysis of a natural jointed rock slope based on the
24 photogrammetry method, *Landslides*, 12(1), 147-154, 2015.

25 Duriez, J., Darve, F., and Donze, F.V.: Incrementally non-linear plasticity applied to rock joint modeling,
26 *International Journal for Numerical and Analytical Methods in Geomechanics*, 37(5), 453-477, 2011.

27 Feng, M., Fredlund, D.G.: Hysteretic influence associated with thermal conductivity sensor measurements, In
28 *Proceedings from Theory to the Practice of Unsaturated Soil Mechanics in Association with the 52nd Canadian*
29 *Geotechnical Conference and the Unsaturated Soil Group*, Regina, Sask, 14(2), 14-20, 1999.

30 Harlow, F.H.: The particle-in-cell computing method for fluid dynamics, *Computer Methods in Physics*, 3, 319-343,
31 1964.

32 He, M.C.: Real-time remote monitoring and forecasting system for geological disasters of landslides and its
33 engineering application (in Chinese), *Chinese Journal of Rock Mechanics and Engineering*, 28(6), 1081-1090,
34 2009.

35 He, M.C., Gong, W.L., Wang, J., Qi, P., Tao, Z.G., Du, S., and Peng, Y.Y.: Development of a novel
36 energy-absorbing bolt with extraordinarily large elongation and constant resistance, *International Journal of Rock*
37 *Mechanics and Mining Sciences*, 67(67), 29-42, 2014.



- 1 Hill, R.: A general theory of uniqueness and stability in elastic-plastic solids, *Journal of the Mechanics and Physics*
- 2 *of Solids*, 6, 236-249, 1958.
- 3 Huang, D., Cen, D.F., Ma, G.W., and Huang, R.Q.: Step-path failure of rock slopes with intermittent joints,
- 4 *Landslides*, 12(5), 911-926, 2015.
- 5 James, J., Conca, A.B., and Judith Wright, A.B.: The UFA method for rapid, direct measurements of unsaturated
- 6 transport properties in soil, sediment, and rock, *Australian Journal of Soil Research*, 36, 291-315, 1998.
- 7 Khoa, H.D.V., Georgopoulos, I.O., Darve, F., and Laouafa, F.: Diffuse failure in geomaterials: experiments and
- 8 modelling, *Computers and Geotechnics*, 33, 1-14, 2006.
- 9 Laouafa, F., Prunier, F., Daouadji, A., Al Gali, H., and Darve, F.: Stability in geomaterials, experimental and
- 10 numerical analyses, *International Journal for Numerical and Analytical Methods in Geomechanics*, 35, 112-139,
- 11 2011.
- 12 Li, Z.H., Dufour, F., and Darve, F.: Hydro-elasto-plastic modelling with a solid/fluid transition, *Computers and*
- 13 *Geotechnics*, 75, 69-79, 2016.
- 14 Li, Z.H., Dufour, F., and Darve, F.: Modelling rainfall-induced mudflows using FEMLIP and a unified
- 15 hydro-elasto-plastic model with solid-fluid transition, *European Journal of Environmental and Civil Engineering*,
- 16 22(4), 491-521, 2018a.
- 17 Li, Z.H., Jiang, Y.J., Tao, Z.G., He, M.C.: Monitoring prediction of a rockslide in an open-pit mine and numerical
- 18 analysis using a material instability criterion, *Bulletin of Engineering Geology and Environment*, published online,
- 19 2018b.
- 20 Lignon, S., Laouafa, F., Prunier, F., Khoa, H.D.V., and Darve, F.: Hydro-mechanical modelling of landslides with a
- 21 material instability criterion, *Géotechnique*, 59(6), 513-524, 2009.
- 22 Marcelo, A., Llano-Serna, M.F., and Dorival, M.P.: An assessment of the material point method for
- 23 modeling large scale run-out processes in landslides, *Landslides*, 13(5), 1057-1066, 2016.
- 24 Ministry of Water Resources and Electric Power of People's Republic of China, Code for Engineering Geological
- 25 Investigation of Water Resources and Hydropower GB50487-2008 (in Chinese), 2008.
- 26 Moresi, L., Dufour, F., and Mühlhaus, H.B.: Mantle convection modeling with viscoelastic/brittle lithosphere:
- 27 numerical methodology and plate tectonic modeling, *Pure and Applied Geophysics*, 159(10), 2335-2356, 2002.
- 28 Moresi, L., Dufour, F., and Mühlhaus, H.B.: A Lagrangian integration point finite element method for large
- 29 deformation modelling of viscoelastic geomaterials, *Journal of Computational Physics*, 184(2), 476-497, 2003.
- 30 Nicot, F., and Darve, F.: Diffuse and localized failure modes: Two competing mechanisms, *International Journal*
- 31 *for Numerical and Analytical Methods in Geomechanics*, 35(5), 586-601, 2011.
- 32 Parlange, J.Y.: Water transport in soils, *Annual Revision of Fluid Mechanics*, 12, 77-102, 1980.
- 33 Prime, N., Dufour, F., and Darve, F.: Unified model for Geomaterial solid/fluid states and the transition in between,
- 34 *Journal of Engineering Mechanics*, 140(6), 682-694, 2013.
- 35 Prunier, F., Laouafa, F., Lignon, S., and Darve, F.: Bifurcation modelling in geomaterial : From the second-order
- 36 work criterion to spectral analyses, *International Journal for Numerical and Analytical Methods in Geomechanics*,
- 37 33(9), 1169-1202, 2009.



- 1 Prunier, F., Chomette, B., Brun, M., and Darve, F.: Designing geotechnical structures with a proper stability
- 2 criterion as a safety factor, *Computers and Geotechnics*, 71, 98-114, 2016.
- 3 Regmi, A.D., Yoshida, K., Dhital, M.R., and Devkota, K.: Erratum to: Effect of rock weathering, clay mineralogy,
- 4 and geological structures in the formation of large landslide, a case study from DumreBesei landslide, Lesser
- 5 Himalaya Nepal, *Landslides*, 9(2), 299-301, 2012.
- 6 Soga, A., Alonso, E., Yerro, A., Kumar, K., and Bandara, S.: Trends in large deformation analysis of landslide mass
- 7 movements with particular emphasis on the material point method, *Géotechnique*, 1-26, 2016
- 8 Sun, D.X., Tao, Z.G., Fan, L.J., and Feng, X.R.: Stability assessment and sensibility analysis of Nanfen open-pit
- 9 mine slope (in Chinese), *Metal Mine*, 5, 57-60, 2011.
- 10 Tu, X.B., Kwong, A.K.L., Dai, F.C., Tham, L.G., and Min, H. Field monitoring of rainfall infiltration in a loess
- 11 slope and analysis of failure mechanism of rainfall-induced landslides, *Engineering Geology*, 105(1-2), 134-150,
- 12 2009.
- 13 Van Eekelen, H.A.M.: Isotropic yield surfaces in three dimensions for use in soil mechanics, *International Journal of*
- 14 *Numerical and Analytical Methods in Geomechanics*, 4, 89-101, 1980.
- 15 Van Genuchten, M.T.: A closed-form equation for predicting the hydraulic conductivity of unsaturated soils, *Soil*
- 16 *Science Society of America Journal*, 44, 892-898, 1980.
- 17 Wang, J.J., Zhang, H.P., Liu, T.: Determine to slip surface in waterfront soil slope analysis, *Advanced Materials*
- 18 *Research*, 378-379, 466-469, 2011.
- 19 Yang, F., Hou, K.P., and Xie, Y.L.: Mechanical parameters determination method for strongly weathered
- 20 mica-quartz schist (in Chinese), *Journal of Chang'an University*, 32(2), 29-38, 2012.
- 21 Zhang, K., Tan, P., Ma, G.W., and Can, P.: Modeling of the progressive failure of an overhang slope subject to
- 22 differential weathering in Three Gorges Reservoir, China, *Landslides*, 13(5), 1303-1313, 2016.